EES Catalysis

Check for updates

Plasma-driven redox mechanism in the reverse water–gas shift reaction over Ni–In intermetallic catalysts†

Dae-Yeong Kim, ✶[a] Zhang Wenjun,[a] Kaiyue Dong,[b] Bang Lu,[b] Duanxing Li,[c] Satoru Takakusagi,[b] Shinya Furukawa[c] and Tomohiro Nozaki[a]

The reverse water–gas shift (RWGS) reaction has been recognized as a promising strategy for CO_2 valorization. However, it faces limitations due to low activity and poor CO selectivity at low temperatures. In this study, we report that plasma can effectively promote the low-temperature RWGS reaction over Ni–In intermetallic catalysts. The formation of the Ni–In intermetallic phases completely suppresses CH_4 formation and achieves 100% CO selectivity. Through *in situ* transmission infrared spectroscopy (TIR) and *in situ* X-ray absorption fine-structure (XAFS) analysis, we monitored the changes occurring on the catalyst surface during the plasma reaction. The interaction between redox-active sites present in the Ni–In intermetallic catalysts and plasma-activated species lowers the activation energy, thereby facilitating the RWGS reaction at low temperatures. This study offers fundamental insights into how plasma-activated species enhance catalysis and the underlying mechanisms of low-temperature activation in plasma catalysis.

Broader context

The accelerating impact of anthropogenic CO_2 emissions has made the development of sustainable carbon recycling technologies a global priority. Among these, the reverse water–gas shift (RWGS) reaction offers a promising route to convert CO_2 into CO, an important intermediate for producing synthetic fuels and chemicals. However, conventional RWGS processes require high operating temperatures due to the thermodynamic stability of CO_2, resulting in high energy input and potential catalyst deactivation. At lower temperatures, CO_2 methanation becomes thermodynamically favorable, reducing CO selectivity. Recent advances in plasma catalysis offer new opportunities to promote catalytic reactions at low temperatures by utilizing nonthermal plasma (NTP), which generates energetic electrons that can activate stable molecules. This study introduces a Ni–In intermetallic catalyst system that, when integrated with NTP, drives the RWGS reaction at low temperatures with 100% CO selectivity. By combining kinetic studies with *in situ* transmission infrared spectroscopy and *in situ* X-ray absorption fine structure analysis, we elucidate the dynamic interplay between plasma-activated species and the redox-active surface of the Ni–In intermetallic catalyst. These investigations provide a rational basis for low-temperature CO_2 conversion using non-noble metal catalysts and highlight a promising route toward electrified chemical manufacturing powered by renewable energy.

Introduction

Over the past few decades, the excessive combustion of fossil fuels has significantly increased CO_2 emissions, contributing to various environmental challenges.[1,2] In this context, the reverse water–gas shift (RWGS) reaction has recently garnered attention as a promising approach for converting CO_2 into CO using green hydrogen.[3–8] The produced CO serves as a key building block for high-value chemicals through Fischer–Tropsch synthesis and other syngas-based processes.[5] Operating the RWGS reaction at low temperatures is advantageous as it helps suppress catalyst sintering and agglomeration, thereby preserving active sites.[9] However, due to the high stability of CO_2 molecules and the endothermic nature of the RWGS reaction, high reaction temperatures are typically required. Moreover, at low temperatures, CO_2 methanation becomes thermodynamically favorable, reducing CO selectivity. Consequently, developing catalyst systems that efficiently promote the RWGS reaction at low temperatures remains a critical challenge.

Recently, plasma catalysis has emerged as an alternative approach, integrating nonthermal plasma (NTP) with catalytic reactions to drive chemical transformations using electrical energy.[10–13] In an NTP environment, the bulk gas temperature

[a] *Department of Mechanical Engineering, Institute of Science Tokyo, Tokyo 152-8550, Japan. E-mail: kim.d.as@m.titech.ac.jp*
[b] *Institute for Catalysis, Hokkaido University, Sapporo 001-0021, Japan*
[c] *Division of Applied Chemistry, Osaka University, Osaka 565-0871, Japan*
† Electronic supplementary information (ESI) available. See DOI: https://doi.org/10.1039/d5ey00101c

remains near room temperature, while accelerated electrons in the electric field reach extremely high energy levels (10^4–10^5 K).[14] These high-energy electrons effectively activate molecules with strong chemical bonds, such as CO_2, CH_4 and N_2, through energetic collisions.[15–17] Consequently, plasma catalysis enables plasma-activated species to interact with catalyst surfaces, lowering energy barriers in key reaction steps and enhancing catalytic performance. Thus, the rational design of high-performance catalysts for plasma-assisted reactions requires a comprehensive understanding of the interactions between plasma-activated species and the catalyst surface.

Meanwhile, noble metal catalysts (*e.g.*, Pt, Rh, Ir and Au) exhibit high activity in low-temperature RWGS reactions,[18–21] but their high cost significantly limits practical applications. In contrast, Ni-based catalysts are widely explored for their cost-effectiveness and catalytic activity in various reactions.[22–24] However, they typically favor CH_4 formation in CO_2 hydrogenation, leading to low CO selectivity. Therefore, developing strategies to shift the selectivity of Ni-based catalysts from CH_4 to CO remains a crucial research challenge. Intermetallic catalysts provide a promising strategy to achieve high activity and selective product formation by tuning the electronic and geometric properties of monometallic catalysts.[25] Recent studies on Ni–In intermetallic catalysts have demonstrated that the incorporation of In can modulate CO_2 activation and conversion pathways, suppressing CH_4 formation while enhancing CO production.[26–29]

In our previous study, we investigated CO_2 hydrogenation over Ni/Al$_2$O$_3$ catalysts and observed 100% CH_4 selectivity under both thermal and plasma conditions. Notably, CH_4 formation was significantly promoted under plasma conditions at low temperatures.[30,31] Given the synergy between Ni/Al$_2$O$_3$ catalysts and plasma, we sought to enhance the low-temperature performance of Ni/Al$_2$O$_3$ catalysts for the RWGS reaction through intermetallic phase engineering. To this end, we focused on incorporating In into the Ni/Al$_2$O$_3$ catalyst to form Ni–In intermetallic phases, aiming to shift product selectivity toward CO in CO_2 hydrogenation. The resulting catalyst was then applied to plasma catalysis. This study aimed to enhance the low-temperature activity and CO selectivity of Ni-based catalysts in the RWGS reaction and to gain mechanistic insights into the plasma-assisted reaction. In this context, we conducted kinetic studies combined with *in situ* transmission infrared spectroscopy (TIR) and *in situ* X-ray absorption fine-structure (XAFS) analyses (where plasma is generated within the cell) to probe the dynamic behavior of the catalyst surface under plasma conditions. The formation of the Ni–In intermetallic phases shifts the reaction pathway from an associative mechanism to a redox mechanism. Furthermore, it suppresses CH_4 formation, facilitating exclusive CO production. Plasma-activated species promote both oxidation and reduction reactions, enabling CO_2 conversion to reach thermodynamic equilibrium even at a relatively low temperature of approximately 450 °C. These findings validate the potential of the Ni–In intermetallic catalysts for selective CO production *via* CO_2 hydrogenation while providing mechanistic insights into low-temperature activity in plasma catalysis.

Experimental section

Catalyst preparation and characterization

The Ni/Al$_2$O$_3$ catalyst were prepared by the deposition–precipitation method with a loading amount of 6 wt%. Aqueous solution of urea was added dropwise to a vigorously stirred mixture of γ-Al$_2$O$_3$ (99.9%, Kojundo Chemical Lab) and an aqueous solution of Ni(NO$_3$)$_2$·6H$_2$O (99%, FUJIFILM Wako) in a glass beaker. The mixture was sealed tightly with a plastic film and heated with stirring on a hot stirrer. The temperature of the mixture was kept at 90 °C for 5 h. After deposition, the colorless supernatant was removed and the resulting solid was washed with deionized water three times, followed by drying under reduced pressure. The resulting powder was calcined in air at 500 °C for 1 h and then reduced at 600 °C under a 50 mL min^{-1} H$_2$ flow for 1 h. The Ni–In/Al$_2$O$_3$ catalyst was prepared in a similar fashion to that of Ni/Al$_2$O$_3$ using a mixed aqueous solution of Ni(NO$_3$)$_2$·6H$_2$O and In(NO$_3$)$_3$·nH$_2$O (99.99%, Kojundo Chemical Lab) with a loading amount of 6 wt% and a Ni/In atomic ratio of 1. The X-ray diffraction (XRD) patterns of Ni/Al$_2$O$_3$ and Ni–In/Al$_2$O$_3$ were recorded by using a MiniFlex 600 + D/teX Ultra2 instrument with a Cu Kα X-ray source. The diffraction peaks assignable to metallic Ni and Ni–In intermetallic phases were observed (Fig. S1, ESI†). The N$_2$ adsorption–desorption isotherms of the Ni–In/Al$_2$O$_3$ catalyst were obtained using a Belsorp-Max (BEL Japan). The BET surface area was calculated to be 70 m^2 g^{-1} (Fig. S2, ESI†). The morphology of the prepared catalysts was observed by transmission electron microscopy (TEM, JEOL, JEM-ARM200F NEOARM, 200 kV). High-angle annular dark-field scanning transmission electron microscopy (HAADF-STEM) combined with energy-dispersive X-ray spectroscopy (EDX) was also performed. The HAADF-STEM images (Fig. S3a, ESI†) show Ni–In nanoparticles dispersed on the Al$_2$O$_3$ support. The corresponding EDX elemental mapping (Fig. S3e, ESI†) confirms that Ni and In are uniformly distributed, indicating strong intermetallic interaction between them due to the formation of a Ni–In intermetallic phase. Collectively, these characterization results confirm the successful formation of the desired Ni–In intermetallic catalyst.

Catalytic reaction

RWGS reaction was conducted in a packed-bed dielectric barrier discharge (DBD) reactor (Fig. S4, ESI†). The reactor consists of a quartz tube (20 mm i.d. × 23 mm o.d.), a high-voltage (HV) electrode (stainless steel; 1 mm i.d. × 6 mm o.d.), and a ground electrode (stainless steel) out-side the quartz tube. HV electrodes were placed coaxially along the reactor axis. The powder catalyst was manufactured in pellets (5 mm diameter, 2 mm thickness). Before RWGS reaction performance evaluation, 8 g catalyst was reduced at 700 °C for 60 min in 10% H$_2$/Ar gas flow (total flow rate = 550 mL min^{-1}). Afterward, the catalyst was packaged in a quartz tube, and a mixture of H$_2$ and CO_2 was introduced through the HV electrode. Ar was bypassed in the reactor and not included in the reaction. The total flow rate and weight hourly space velocity (WHSV) of the mixture of H$_2$ and CO_2 (molar ratio 3:1) were 400 mL min^{-1} and 3000 mL g^{-1} h^{-1}, respectively, under standard

temperature and pressure (STP) conditions (25 °C and 101 kPa). The total pressure was fixed at 30 kPa. DBD was generated using AC high-voltage power (Logy Electric; LHV-13AC, 12 kHz and ASTECH; LG-10S RF Generator, 100 kHz). The applied voltage and average current were measured with an oscilloscope (Agilent Technologies, DSO-X 3014A). The discharge power was obtained by the voltage-charge Lissajous figure method (Fig. S5, ESI†) and was fixed at 40 W, according to the following equation:

$$P = f \oint Q \mathrm{d}V$$

where P (W) is the discharge power, f (kHz) is the applied frequency, Q (nC) is the charge, and V (kV) is the applied voltage.

The catalyst temperature was measured with an infrared camera coupled with an IR reflector (TH5104, NEC Sanei Instrument, Ltd). The infrared camera was calibrated with a thermocouple without DBD. Meanwhile, the catalyst temperature can vary locally due to factors such as the endothermic (or exothermic) nature of the reaction and heating induced by plasma, which may result in a temperature difference between the reactor wall and the catalyst bed. Therefore, during thermal and plasma reactions, the catalyst temperature was determined based on measurements at five different locations within the catalyst bed instead of the reactor wall temperature (see Fig. S4, ESI†). To reach the target reaction temperatures (350–500 °C), an external furnace was employed during both thermal and plasma conditions, since plasma heating alone could not increase the catalyst temperature above 300 °C.

Specific energy input (SEI) was calculated by following formula:

$$\mathrm{SEI} = \frac{\mathrm{Power}}{e N_\mathrm{A} \times \dfrac{Q_\mathrm{total}^\mathrm{in}}{60 \times 10^6} \times \dfrac{P}{RT}}$$

$Q_\mathrm{total}^\mathrm{in}$ (mL min^{-1}, STP) represents the total gas flow rate at STP conditions (25 °C and 101 kPa). T and P refer to the catalyst temperature and reaction pressure respectively. e and N_A represent elementary charge (C) and Avogadro number (mol^{-1}). SEI represents the mean discharge energy input per molecule (eV per molecule). The calculated SEI for the reaction gas (a mixture of H_2 and CO_2) was 1.5 eV per molecule. Quantitative gas analysis was performed by quadrupole mass spectrometry (QMS, Prisma Plus QMG220). The CO_2 conversion, and CO selectivity were calculated as follows:

$$CO_2 \text{ conversion}\% = \frac{F_{CO_2}^\mathrm{in} - F_{CO_2}^\mathrm{out}}{F_{CO_2}^\mathrm{in}} \times 100$$

$$CO \text{ selectivity}\% = \frac{F_{CO}^\mathrm{out}}{F_{CO_2}^\mathrm{in} - F_{CO_2}^\mathrm{out}} \times 100$$

$$CH_4 \text{ selectivity}\% = \frac{F_{CH_4}^\mathrm{out}}{F_{CO_2}^\mathrm{in} - F_{CO_2}^\mathrm{out}} \times 100$$

$$\text{Carbon balance}\% = \frac{F_{CO}^\mathrm{out} + F_{CH_4}^\mathrm{out} + F_{CO_2}^\mathrm{out}}{F_{CO_2}^\mathrm{in}} \times 100$$

F (mol min^{-1}) expresses mol flow rate at STP conditions. The carbon balance was 100% under both thermal and plasma conditions, indicating that no significant carbon deposition occurred under both thermal and plasma conditions.

In situ TIR

The *in situ* TIR analysis under thermal and plasma conditions was measured using a DBD flow-type TIR cell (Fig. S6, ESI†). The TIR cell was in the form of a cylindrical glass tube. The HV and ground electrodes (stainless steel; 1 mm diameter) were inserted inside the reactor and the ground electrode was wrapped in a quartz sheath. The gap between point-to-point electrodes was 10 mm. A HV supply was connected to the reactor and discharge power and frequency for all catalyst tests were 0.001 W and 19 kHz, respectively and kept constant. The powder catalyst (40 mg) was manufactured in a pellet (10 mm diameter, 1 mm thickness). After that, the catalyst pellet was fixed in a glass holder and inserted into the 5 mm downstream from the plasma discharge zone. The *in situ* TIR spectra was collected using a Fourier-transform infrared spectrometer (FTIR, JASCO FTIR-6100) equipped with a mercury cadmium telluride (MCT) detector with a spectral resolution of 4 cm^{-1}. Before spectral acquisition, the catalyst pellet was reduced at 700 °C under a 10% H_2/Ar flow for 1 h. For measurement, the gas flows of CO_2, H_2, and Ar were 10 mL min^{-1}, 30 mL min^{-1}, and 60 mL min^{-1}, respectively.

In situ XAFS

The Ni and In K-edge XAFS measurements of the Ni–In/Al$_2$O$_3$ catalysts were carried out at the BL9A beamline of the photon factory (PF) and at the NW10A beamline of the photon factory advanced ring (PF-AR), respectively, in the Institute of material structure science (IMSS) of high energy accelerator research organization (KEK). Si(111) and Si(311) monochromators were used for the Ni and In K-edge XAFS measurements, respectively. The spectra were recorded in transmission mode using the same cell as for *in situ* TIR (Fig. S6, ESI†). Before spectral acquisition, the catalyst pellet was reduced at 700 °C under a 25% H_2/Ar flow for 1 h. For the XAFS measurements, the gas flows of CO_2, H_2, and Ar were 20 mL min^{-1}, 60 mL min^{-1}, and 60 mL min^{-1}, respectively, and the reaction temperature was set at 350 °C. The XANES spectra were normalized to their edge height after background subtraction. The EXAFS spectra were analyzed using the RIGAKU REX2000 software.[32] The EXAFS oscillations ($\chi(k)$) were extracted using a spline smoothing method and normalized to their edge height after background subtraction, where k is the photoelectron wavenumber and calculated from the photon energy, E, using the equation (1).

$$k = \sqrt{\frac{2m_\mathrm{e}(E - E_0)}{\hbar^2}} \tag{1}$$

E_0 and m_e are the threshold energy and the electron mass, respectively. The quantity of $k^3\chi(k)$ in the k-range of 3.0–12.0 Å^{-1} was Fourier transformed into R-space. We did not show the results of the curve fitting EXAFS analysis for the following two reasons. 1. The crystal structures of the Ni–In

alloys ($NiIn$ and Ni_2In_3 phases) indicate that the Ni–In bond distance has a large asymmetric (non-Gaussian) distribution (2.62–2.77 Å). This causes significant destructive interference between the corresponding Ni–In EXAFS oscillations and gives a much smaller coordination number for the Ni–In interaction than the actual one, which is confirmed by our preliminary curve fitting results for the Ni–In/Al_2O_3 catalysts. 2. The maximum number of the fitting parameters (N_p) available was estimated to be ~ 8 based on the Nyquist criterion,[33] $M \approx 2\Delta k \Delta R/\pi$ where N_p should be smaller than M. Δk and ΔR are the range of the Fourier transform and the range over which the fit is evaluated, respectively. Considering that four structural parameters are required, *i.e.* bond distance, coordination number, energy shift, and Debye–Waller factor, for each bond in the curve fitting analysis, the fitting with three different bonds such as Ni–In, Ni–Ni and Ni–O is not allowed due to the limitation of N_p. We have found that such fittings were not reliable, even when some structural parameters were fixed.

Results and discussion

The catalytic performance of the synthesized Ni–In intermetallic catalysts under thermal and plasma conditions was evaluated in a packed-DBD reactor (Fig. S4, ESI†) by supplying an H_2/CO_2 mixed gas (molar ratio 3 : 1). As shown in Fig. 1(a) and (b), under both thermal and plasma conditions, the CO_2 conversion steadily increased with temperature, while maintaining 100% CO selectivity, confirming the excellent CO selectivity of Ni–In/Al_2O_3. According to our previous study and reported literature,[30,34,35] Ni/Al_2O_3 typically favors CH_4 formation. However, the formation of the Ni–In intermetallic phases suppresses this tendency toward CH_4 formation. Meanwhile, CO_2 conversion significantly increased under plasma conditions, with the plasma promotion effect being particularly pronounced at 100 kHz. Specifically, at 400 °C, the CO_2 conversion under thermal conditions was only about 10%, whereas under plasma conditions at 100 kHz, the conversion approached the upper limit of thermodynamic equilibrium, and at 450 °C, it reached thermodynamic equilibrium.

To understand the enhancement in activity under plasma conditions, kinetic experiments were conducted to investigate the apparent activation energy (see ESI† Note 1 for details). As shown in Fig. 1(c), a good linear relationship was observed between the reaction rate constant (k) and the inverse absolute temperature ($1/T$) under both thermal and plasma conditions. Using the Arrhenius equation, the apparent activation energy (E_A) was derived, revealing a clear decrease in E_A under plasma conditions.

Interestingly, while the E_A values at 12 kHz and 100 kHz under plasma conditions were similar, the k value was higher at 100 kHz. This can be explained by an increase in the pre-exponential factor. At higher frequencies, the number of streamers per unit time increases, leading to a significant rise in the total discharge current and, consequently, an increase in the total amount of plasma active species.[36] In other words, more plasma-active species are generated at 100 kHz, resulting in an increase in the pre-exponential factor and, consequently, an accelerated reaction rate. These results suggest that plasma-active species play a crucial role in promoting reactions on the catalyst surface. To elucidate the RWGS reaction mechanism under thermal conditions and the promotion effect induced by plasma, *in situ* TIR analyses were conducted at 350 °C. Generally, two major reaction mechanisms have been proposed for the RWGS reaction: the redox mechanism and the associative mechanism.[37–39] In the redox mechanism, CO_2 is directly dissociated on the catalyst surface, producing CO and oxidized species. In this case, H_2 does not directly participate in CO_2 reduction but instead plays a role in reducing the oxidized species to restore the catalyst to its initial state. On the other hand, in the associative mechanism, CO_2 and H_2 react to form formate species, which subsequently decompose to generate CO. Since these two mechanisms involve different reaction steps in the CO_2 activation process, a transient experiment can be an appropriate approach to elucidate the RWGS reaction mechanism and investigate the catalytic surface dynamics of plasma-activated CO_2 and H_2. Accordingly, we recorded time-resolved TIR spectra while alternating the CO_2 and H_2 flow every 10 min.
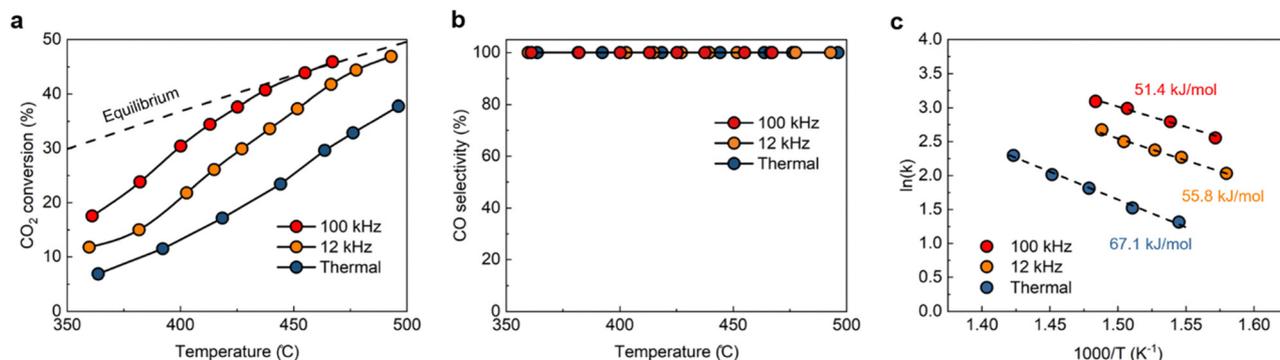

Fig. 1 RWGS activity under thermal and plasma conditions over Ni–In/Al_2O_3. (a) Temperature-dependent CO_2 conversion and (b) CO selectivity. Reaction conditions: total flow rate = 400 mL min^{-1} (STP); H_2/CO_2 = 3; WHSV 3000 mL g^{-1} h^{-1} (STP); pressure = 30 kPa; SEI = 1.5 eV per molecules. (c) Arrhenius plots. When calculating the k value, the reaction was under a kinetically controlled regime (CO_2 conversion was lower than 20%) by adjusting the WHSV, as detailed in the (ESI†).
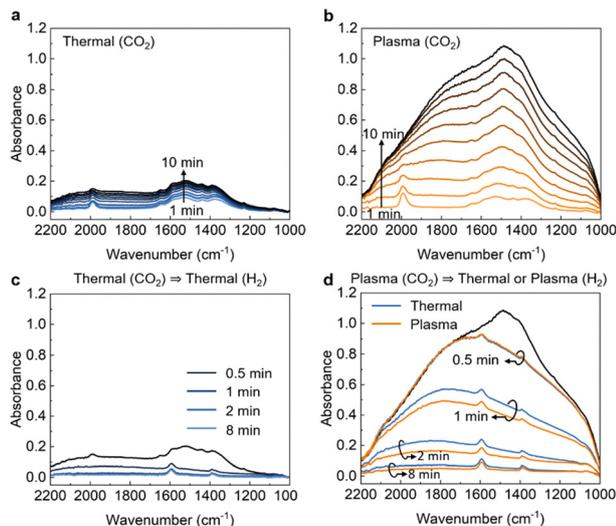
Fig. 2 Investigation of the reaction mechanism over Ni–In/Al$_2$O$_3$. *In situ* TIR spectra recorded at 350 °C during CO$_2$ exposure under (a) thermal and (b) plasma conditions, and after switching from CO$_2$ to H$_2$ under (c) thermal-to-thermal and (d) plasma-to-thermal or plasma conditions.

As shown in Fig. 2(a), under thermal conditions, exposure to CO$_2$ results in the appearance of a signal around 2000 cm^{-1}, corresponding to linearly adsorbed CO on Ni^0 (l-CO*).[40] This peak is red-shifted relative to that observed for monometallic Ni catalysts (2050–2100 cm^{-1}),[41] which is attributed to the inter-metallic effect with In. Specifically, the formation of the Ni–In intermetallic phases alters the electron density of Ni, enhancing π-back donation, which in turn elongates the C≡O bond and weakens CO adsorption. The reduced CO adsorption strength suppresses further hydrogenation reactions on the catalyst surface, ultimately leading to high CO selectivity (Fig. 1(b)). Meanwhile, in addition to l-CO*, peaks related to carbonate species were also observed in the 1700–1200 cm^{-1} region. As the CO$_2$ exposure time increased, the l-CO* signal gradually decreased, while IR absorbance in the 2200–1000 cm^{-1} range increased. This increase in absorbance serves as evidence of Ni–In oxidation. To confirm this, we introduced O$_2$ gas to induce Ni–In oxidation and observed spectral changes (Fig. S10, ESI†), showing a pronounced increase in absorbance in the 2200–1000 cm^{-1} range. This absorbance increase under the same CO$_2$ flow conditions was not observed for Ni/Al$_2$O$_3$ catalysts (Fig. S11, ESI†). In other words, the absorbance increase in the 2200–1000 cm^{-1} region originates from the oxidation of In and may correspond to an overtone of the skeletal vibration of In–O. Based on these results, it can be interpreted that CO$_2$ undergoes a deoxygenation reaction on the Ni–In surface to form l-CO*, while simultaneously inducing oxidation of Ni–In. On the other hand, under plasma conditions (Fig. 2(b)), a relatively sharp l-CO* initially appears. As the CO$_2$ flow continues over time, l-CO* gradually decreases, while the increase in absorbance in the 2200–1000 cm^{-1} region becomes even more pronounced. No spectral difference was observed in the gas-phase CO region (2250–2050 cm^{-1}) between thermal and plasma conditions.

This absence of gas-phase CO bands suggests that direct dissociation of CO$_2$ by plasma can be ruled out. That is, the distinct spectral differences relative to thermal conditions indicate that plasma-activated CO$_2$ promotes surface oxidation reactions. Furthermore, along with the increase in absorbance in the 2200–1000 cm^{-1} range, peaks corresponding to carbonate species in the 1700–1200 cm^{-1} region also increased relative to thermal conditions. This suggests that they are formed through the reaction between oxidized catalyst O* species and CO$_2$.

Subsequently, upon switching to an H$_2$ atmosphere under thermal conditions (Fig. 2(c)), l-CO* rapidly decreases, indicating that H$_2$ competitively adsorbs with l-CO* on the catalyst surface. Additionally, the IR absorbance in the 2200–1000 cm^{-1} range, which had increased in the CO$_2$ atmosphere, decreases, signifying the reduction of Ni–In that had been oxidized under CO$_2$ exposure. Meanwhile, along with the decrease in carbonate species observed in the 1700–1200 cm^{-1} region, peaks attributed to formate species appeared at 1595, 1392 and 1378 cm^{-1},[38] suggesting that carbonate species were converted into formate species. Furthermore, formate species showed little change over time in the H$_2$ atmosphere, identifying it as a spectator. To gain insight into plasma-activated H$_2$ under H$_2$ flow, we compared spectra obtained under thermal and plasma conditions after plasma CO$_2$ exposure. As shown in Fig. 2(d), after 0.5 min of H$_2$ exposure, carbonate species rapidly converted to formate species. The difference induced by plasma becomes evident after 1 min, where the absorbance in the 2200–1000 cm^{-1} region decreases more rapidly under plasma conditions than under thermal conditions. This suggests that the catalyst, which had been oxidized, was reduced by plasma-activated H$_2$ and that plasma promotes not only oxidation but also the reduction process.

Meanwhile, no significant changes in the formate species peak were observed under plasma conditions, further confirming that formate species is a spectator. This observation aligns with previous studies, which have reported that formate species primarily behave as a spectator in redox mechanisms.[38,39]

Next, *in situ* XAFS characterization was performed at 350 °C to gain deeper insight into the chemical state of the Ni–In intermetallic catalyst. Prior to the experiment, the catalyst was reduced, and both Ni and In were confirmed to be in their metallic states by the *in situ* Ni and In K-edge X-ray absorption near edge structure (XANES) measurements (Fig. S13, ESI†), as the corresponding absorption edge energies were similar to those of Ni and In foils, respectively. The X-ray absorption near edge structure (XANES) and extended X-ray absorption fine structure (EXAFS) spectra are presented in Fig. 3 and Fig. S14 (ESI†), respectively. Under thermal conditions, the Ni K-edge XANES spectra show that, when the reaction gas is switched from CO$_2$ + H$_2$ to CO$_2$ alone (Fig. 3(a)), the spectral features change to resemble those of Ni foil. For the In K-edge XANES, the white line intensity was slightly increased, indicating that metallic In is slightly oxidized under a CO$_2$ atmosphere. In the Ni K-edge EXAFS spectra (Fig. S14a, ESI†), a distinct contribution from Ni–Ni scattering appears at around 2.1 Å after the gas
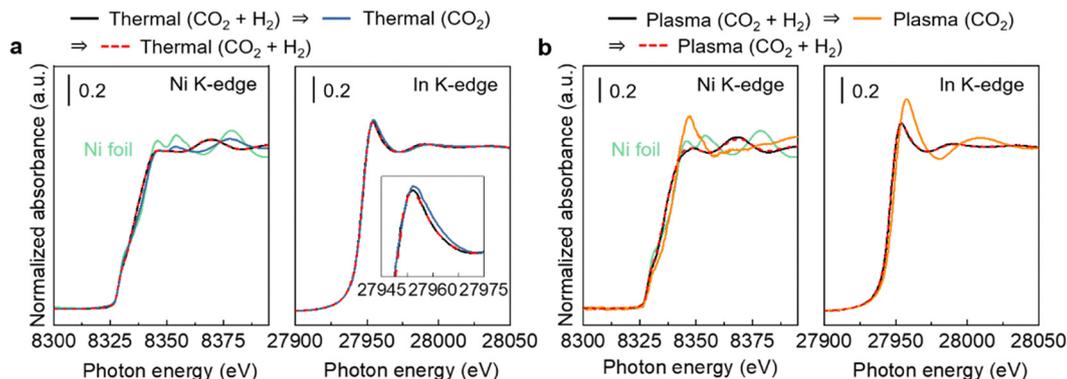
Fig. 3 *In situ* Ni and In K-edge XANES spectra of Ni–In/Al$_2$O$_3$ recorded at 350 °C under (a) thermal and (b) plasma conditions during CO$_2$ + H$_2$, after switching to CO$_2$, and subsequently returning to CO$_2$ + H$_2$.

switch. As shown in the In K-edge EXAFS spectra (Fig. S14b, ESI†), the contribution from In–Ni scattering at around 2.2 Å decreases, and a new In–O scattering contribution emerges at around 1.6 Å. Meanwhile, under plasma conditions, switching to CO$_2$ alone results in more pronounced changes in the Ni and In K-edge XANES spectra, increasing the white line intensities and slightly shifting the absorption edge energies to the higher energy side (Fig. 3(b)). In the In K-edge EXAFS spectra (Fig. S14d, ESI†), the In–O contribution becomes more intense. In contrast, the Ni K-edge EXAFS spectra (Fig. S14c, ESI†) still show a Ni–Ni scattering contribution, suggesting that In is preferentially oxidized, followed by the gradual oxidation of Ni. These findings suggest that, under a CO$_2$ atmosphere, the Ni–In intermetallic phase undergoes phase segregation into a quasi Ni-core/In-shell structure as In is oxidized, likely driven by its high oxophilicity and mobility,[42] with oxygen atoms binding to the surface of the In shell. This transformation proceeds more rapidly and strongly under plasma conditions, indicating that plasma-activated CO$_2$ strongly promotes the oxidation of In, followed by the oxidation of Ni. Under thermal conditions, the structural changes induced by CO$_2$ exposure are fully reversed upon H$_2$ reintroduction, as indicated by the red dashed line in Fig. 3(a). This observation supports the reversible redox behavior of the Ni–In intermetallic catalyst, as also inferred from the *in situ* TIR analysis. Furthermore, under plasma conditions, complete structural recovery is also observed upon H$_2$ reintroduction, as indicated by the red dashed line in Fig. 3(b). This result suggests that, although plasma-activated CO$_2$ promotes oxidation, the simultaneous presence of plasma-activated H$_2$ promotes reduction, thereby allowing the Ni–In intermetallic phase to remain dynamically stable.

Taking into account the kinetic study, *in situ* TIR and *in situ* XAFS results, we propose that the Ni–In intermetallic catalysts operate *via* a redox mechanism. In our previous study, CO$_2$ methanation over the Ni/Al$_2$O$_3$ catalyst was confirmed to proceed through an associative mechanism (formate pathway).[30] The formation of the Ni–In intermetallic phases leads to significantly different reaction orders with respect to H$_2$. For Ni/Al$_2$O$_3$, the reaction order of H$_2$ was 0.31, whereas for Ni–In/Al$_2$O$_3$, it was −1.0 (Fig. S8, ESI†).

This indicates that the presence of In^0 species, which can directly reduce CO$_2$ and form In$_2$O$_3$, shifts the reaction mechanism from an associative mechanism to a redox mechanism. Moreover, CH$_4$-related IR peaks, such as those at 1304 and 3015 cm^{-1}, which are observed in CO$_2$ methanation over Ni/Al$_2$O$_3$,[30] were absent under both thermal and plasma conditions with the Ni–In catalyst (Fig. 2 and Fig. S12, ESI†). This supports the suppression of CH$_4$ formation and aligns with the proposed shift in mechanism from associative to redox. The reaction order of −1.0 for H$_2$ can be interpreted as resulting from the competitive adsorption of H$_2$ with CO,[43] as observed in the *in situ* TIR results (Fig. 2).

Meanwhile, when plasma was applied, there was no significant change in the reaction order (Fig. S8, ESI†), suggesting that plasma does not alter the reaction mechanism itself. In other words, vibrationally excited CO$_2$ and atomic hydrogen, which are abundantly generated in DBD,[16,30,44] are responsible for promoting oxidation and reduction reactions, thereby lowering E_A. In the proposed redox mechanism, Ni serves as the active site for CO$_2$ dissociation and CO formation, while In modulates the electronic environment of Ni, suppresses CH$_4$ formation, and participates in the redox cycle through reversible oxidation and reduction. The HAADF-STEM images of the catalyst after the plasma reaction (Fig. S15a, ESI†) revealed no significant morphological changes compared to the fresh sample (Fig. S3a, ESI†). EDX analysis (Fig. S15e, ESI†) showed a shift in the Ni/In molar ratio compared to the fresh sample (Fig. S3e, ESI†), suggesting that the composition of the intermetallic phase may have changed during the plasma reaction. The observed ratio is consistent with the formation of the Ni$_2$In phase and may reflect dynamic structural evolution under plasma conditions. This compositional shift observed by EDX is in good agreement with the *in situ* XAFS results, which suggest that under specific plasma conditions (*e.g.*, CO$_2$ alone), oxidative segregation of In may occur, leading to the formation of Ni–In intermetallic phases with slightly varied compositions.

Conclusions

In summary, we propose plasma-activated Ni–In intermetallic catalysts to enhance the performance of the RWGS reaction at low temperatures. Compared to thermal conditions, plasma

activation significantly improves CO_2 conversion at lower temperatures while maintaining 100% CO selectivity and achieving thermodynamic equilibrium at 450 °C. In addition to kinetic studies, we closely monitored the complex dynamic changes occurring on the catalyst surface under both thermal and plasma conditions through *in situ* TIR and *in situ* XAFS analyses. These findings clearly demonstrate the promotion effect of plasma on the Ni–In intermetallic catalysts, highlighting the crucial role of redox-active sites provided by the Ni–In intermetallic phases in interacting with plasma-activated species. This study provides a fundamental understanding of plasma-driven redox catalysis, which can be extended to other plasma-assisted CO_2 hydrogenation reactions.

Author contributions

D.-Y. K., S. F., S. T. and T. N. wrote the manuscript; D. L. and S. F. synthesized the catalysts and performed the catalysts characterization; D.-Y. K. and T. N. organized kinetic studies and *in situ* TIR analysis. K. D., B. L. and S. T. conducted *in situ* XAFS analysis. All authors contributed to data analysis, interpreted the data, and approved the final version for submission.

Conflicts of interest

There are no conflicts to declare.

Data availability

The date supporting this article have been included in ESI.†

Acknowledgements

References

1 C. Hepburn, E. Adlen, J. Beddington, E. A. Carter, S. Fuss, N. Mac Dowell, J. C. Minx, P. Smith and C. K. Williams, *Nature*, 2019, **575**, 87–97.

2 H.-J. Kim, K. Mori, S. Ichikawa, T. Nakano and H. Yamashita, *Nat. Commun.*, 2025, **16**, 2697.

3 Y. Choi, G. D. Sim, U. Jung, Y. Park, M. H. Youn, D. H. Chun, G. B. Rhim, K. Y. Kim and K. Y. Koo, *Chem. Eng. J.*, 2024, **492**, 152283.

4 M. Ahmadi Khoshooei, X. Wang, G. Vitale, F. Formalik, K. O. Kirlikovali, R. Q. Snurr, P. Pereira-Almao and O. K. Farha, *Science*, 2024, **384**, 540–546.

5 M. González-Castaño, B. Dorneanu and H. Arellano-García, *React. Chem. Eng.*, 2021, **6**, 954–976.

6 M. Juneau, M. Vonglis, J. Hartvigsen, L. Frost, D. Bayerl, M. Dixit, G. Mpourmpakis, J. R. Morse, J. W. Baldwin and H. D. Willauer, *Energy Environ. Sci.*, 2020, **13**, 2524–2539.

7 H.-X. Liu, S.-Q. Li, W.-W. Wang, W.-Z. Yu, W.-J. Zhang, C. Ma and C.-J. Jia, *Nat. Commun.*, 2022, **13**, 867.

8 R. Yamano, S. Ogo, N. Nakano, T. Higo and Y. Sekine, *EES Catal.*, 2023, **1**, 125–133.

9 W. Li, J. Gan, Y. Liu, Y. Zou, S. Zhang and Y. Qu, *Angew. Chem., Int. Ed.*, 2023, **135**, e202305661.

10 A. Bogaerts, X. Tu, J. C. Whitehead, G. Centi, L. Lefferts, O. Guaitella, F. Azzolina-Jury, H.-H. Kim, A. B. Murphy and W. F. Schneider, *J. Phys. D: Appl. Phys.*, 2020, **53**, 443001.

11 T. Nozaki, D.-Y. Kim and X. Chen, *Jpn. J. Appl. Phys.*, 2024, **63**, 030101.

12 T. Nozaki, X. Chen, D.-Y. Kim and C. Zhan, *Plasma Chem. Plasma Process.*, 2023, **43**, 1385–1410.

13 D.-Y. Kim, A. Saito, K. Sasaki and T. Nozaki, *Plasma Sources Sci. Technol.*, 2022, **31**, 124005.

14 J. C. Whitehead, *J. Phys. D: Appl. Phys.*, 2016, **49**, 243001.

15 Z. Sheng, Y. Watanabe, H.-H. Kim, S. Yao and T. Nozaki, *Chem. Eng. J.*, 2020, **399**, 125751.

16 D.-Y. Kim, H. Ham, X. Chen, S. Liu, H. Xu, B. Lu, S. Furukawa, H.-H. Kim, S. Takakusagi and K. Sasaki, *J. Am. Chem. Soc.*, 2022, **144**, 14140–14149.

17 Y. Wang, W. Yang, S. Xu, S. Zhao, G. Chen, A. Weidenkaff, C. Hardacre, X. Fan, J. Huang and X. Tu, *J. Am. Chem. Soc.*, 2022, **144**, 12020–12031.

18 H.-X. Liu, J.-Y. Li, X. Qin, C. Ma, W.-W. Wang, K. Xu, H. Yan, D. Xiao, C.-J. Jia and Q. Fu, *Nat. Commun.*, 2022, **13**, 5800.

19 S. Li, Y. Xu, H. Wang, B. Teng, Q. Liu, Q. Li, L. Xu, X. Liu and J. Lu, *Angew. Chem., Int. Ed.*, 2023, **62**, e202218167.

20 A. I. Rabee, D. Zhao, S. Cisneros, C. R. Kreyenschulte, V. Kondratenko, S. Bartling, C. Kubis, E. V. Kondratenko, A. Brückner and J. Rabeah, *Appl. Catal., B*, 2023, **321**, 122083.

21 S. Li, Y. Xu, Y. Chen, W. Li, L. Lin, M. Li, Y. Deng, X. Wang, B. Ge and C. Yang, *Angew. Chem., Int. Ed.*, 2017, **129**, 10901–10905.

22 M. S. Frei, C. Mondelli, R. García-Muelas, J. Morales-Vidal, M. Philipp, O. V. Safonova, N. López, J. A. Stewart, D. C. Ferré and J. Pérez-Ramírez, *Nat. Commun.*, 2021, **12**, 1960.

23 F. Studt, I. Sharafutdinov, F. Abild-Pedersen, C. F. Elkjær, J. S. Hummelshøj, S. Dahl, I. Chorkendorff and J. K. Nørskov, *Nat. Chem.*, 2014, **6**, 320–324.

24 J. Ma, F. Xing, K.-i Shimizu and S. Furukawa, *Chem. Sci.*, 2024, **15**, 4086–4094.

25 Y. Nakaya and S. Furukawa, *Chem. Rev.*, 2022, **123**, 5859–5947.

26 J. Guo, Z. Wang, J. Li and Z. Wang, *ACS Catal.*, 2022, **12**, 4026–4036.

27 S. Zhang, H. Ma, L. Jia, Z. Zhang, X. Li, S. Dang, Y. Huang, Y. Tian, W. Tu and Y.-F. Han, *Appl. Catal., B*, 2025, **361**, 124646.

28 Z. Xiao, C. Zhang, J. Gu, E. Yuan, G. Li, J.-J. Zou and D. Wang, *Chem. Eng. J.*, 2025, 160529.

29 Y. Zang, X. Lin, J. Qu, F. Gao, J. Gu, T. Wei and S. Zheng, *Int. J. Hydrogen Energy*, 2025, **109**, 295–305.

30 D.-Y. Kim, Y. Inagaki, T. Yamakawa, B. Lu, Y. Sato, N. Shirai, S. Furukawa, H.-H. Kim, S. Takakusagi and K. Sasaki, *JACS Au*, 2024, **5**(1), 169–177.

31 W. Zhang, T. Mimbu, D.-Y. Kim, S. Furukawa, H.-H. Kim and T. Nozaki, *Chem. Eng. J.*, 2025, 162520.

32 T. Taguchi, T. Ozawa and H. Yashiro, *Phys. Scr.*, 2005, **2005**, 205.

33 L. Brillouin, *Science and information theory*, 1962.

34 G. Garbarino, C. Wang, T. Cavattoni, E. Finocchio, P. Riani, M. Flytzani-Stephanopoulos and G. Busca, *Appl. Catal., B*, 2019, **248**, 286–297.

35 J. Lin, C. Ma, Q. Wang, Y. Xu, G. Ma, J. Wang, H. Wang, C. Dong, C. Zhang and M. Ding, *Appl. Catal., B*, 2019, **243**, 262–272.

36 Z. Sheng, K. Sakata, Y. Watanabe, S. Kameshima, H.-H. Kim, S. Yao and T. Nozaki, *J. Phys. D: Appl. Phys.*, 2019, **52**, 414002.

37 E. Pahija, C. Panaritis, S. Gusarov, J. Shadbahr, F. Bensebaa, G. Patience and D. C. Boffito, *ACS Catal.*, 2022, **12**, 6887–6905.

38 L. F. Bobadilla, J. L. Santos, S. Ivanova, J. A. Odriozola and A. Urakawa, *ACS Catal.*, 2018, **8**, 7455–7467.

39 W. Bi, J. Wang, R. Zhang, Q. Ge and X. Zhu, *ACS Catal.*, 2024, **14**, 11205–11217.

40 M. S. Németh, F. Somodi and A. Horváth, *J. Phys. Chem. C*, 2019, **123**, 27509–27518.

41 C. Vogt, E. Groeneveld, G. Kamsma, M. Nachtegaal, L. Lu, C. J. Kiely, P. H. Berben, F. Meirer and B. M. Weckhuysen, *Nat. Catal.*, 2018, **1**, 127–134.

42 H. Eliasson, Y. T. Chiang, T. P. Araújo, X. Li, R. Erni, S. Mitchell and J. Pérez-Ramírez, *Adv. Mater.*, 2025, 2419859.

43 I. C. t Have, J. J. Kromwijk, M. Monai, D. Ferri, E. B. Sterk, F. Meirer and B. M. Weckhuysen, *Nat. Commun.*, 2022, **13**, 324.

44 Z. Sheng, H.-H. Kim, S. Yao and T. Nozaki, *Phys. Chem. Chem. Phys.*, 2020, **22**, 19349–19358.